Leak-Rate Through Carbon Brush Seals: Experimental Tests Versus Predictions From a Porous Medium Approach

Ala Souissi, Mihaï Arghir, Didier Lasseux, Lassad Amami, Philippe Burlot

J. Fluids Eng., **147(4),** 041203, doi : 10.1115/1.4066942

Ala Souissi
Institut PPRIME, UPR CNRS 3346,
Université de Poitiers, ISAE ENSMA,
11 Bd. Marie et Pierre Curie, Bât. H1,
Chasseneuil du Poitou 86360, France
e-mail: ala.eddine.souissi@univ-poitiers.fr

Mihai Arghir
Fellow ASME
Institut PPRIME, UPR CNRS 3346,
Université de Poitiers, ISAE ENSMA,
11 Bd. Marie et Pierre Curie, Bât. H1,
Chasseneuil du Poitou 86360, France
e-mail: mihai.arghir@univ-poitiers.fr

Didier Lasseux
Université de Bordeaux, CNRS, Bordeaux INP,
I2M, UMR 5295,
351, cours de la Libération,
Talence 33405, France
e-mail: didier.lasseux@u-bordeaux.fr

Lassad Amami
Cetim,
74 Rte de la Jonelière,
Nantes 44300, France
e-mail: Lassad.Amami@cetim.fr

Philippe Burlot
Technetics Group,
90 Rue de la Roche du Geai,
Saint-Etienne 42000, France
e-mail: Philippe.Burlot@technetics.com

Leak-Rate Through Carbon Brush Seals: Experimental Tests Versus Predictions From a Porous Medium Approach

This study presents a detailed comparative analysis between experimental leakage flow rates and numerical predictions for carbon brush seals with long bristles, utilizing a porous medium model approach. A series of tests were carried out on a static rig (without rotor rotation). The experimental setup allows tests under various interference conditions, revealing significant insights into the flow behavior through the brush seal. A numerical model based on the Darcy–Forchheimer equation is developed to interpret the complex flow dynamics within the brush seal, accounting for viscous, compressible, and inertial effects. The study evaluates the impact of brush deformation and porosity on flow resistance, leveraging experimental data to refine the numerical model parameters. This investigation not only deepens the understanding of brush seal flow physics but also improves the predictive accuracy of the numerical model in simulating operational conditions.
[DOI: 10.1115/1.4066942]

1 Introduction

Brush seals represent a sealing technology used in rotating machinery and offering advantages over traditional labyrinth seals.

The key benefits of brush seals lie in their remarkable efficiency in minimizing leakage and a cost advantage in some applications [1]. For example, due to their compliant nature, they are able to accommodate important dynamic radial displacements of the rotor that would otherwise lead to damaging contacts in labyrinth seals. Their use brings a significant reduction in weight and space requirements, making these seals particularly attractive for aerospace applications. These characteristics make them attractive even for stationary parts in turbomachinery like compressors and turbines.

Figure 1 depicts a carbon brush seal before and after mounting. The sealing of liquid or gas by a brush seal is ensured by a multitude of deformable bristles forming a compact brush compressed between a front and a back plate at one end and in permanent contact with the rotor at the opposite end. The length of the brush exceeding the radial clearance is called interference which approximately corresponds to the length of the bristles laying on the rotor surface. The contact occurring between the brush and the rotor raises many tribological problems related to friction and wear.

Three types of brush seals can be distinguished following the material employed for the bristles: metallic, Kevlar, or carbon bristles. The bristles material is of capital importance but is not the only design characteristic.

Haynes 25 metallic brush seals have bristles made of a cobalt-based alloy with diameters of the order of 0.07 mm, designed for high strength and oxidation resistance [2]. They operate at temperatures exceeding 700 °C, suitable for the demanding conditions of gas turbines. They are characterized by 100 or 200 bristles per circumferential millimeter mounted with an inclined layout and are engineered to accommodate small radial interferences, up to 0.3 mm between the bristle tip and the rotor surface. Therefore, they can enable thermal expansions without compromising their integrity [3]. Their design is crucial for maintaining effective sealing in dynamic environments (i.e., rotor vibrations), with special attention to wear and heat control.

There are many methods for calculating the flow rate in metallic brush seals. Some are approximate methods relying strongly on experimental data [4–6], while others are more elaborate models

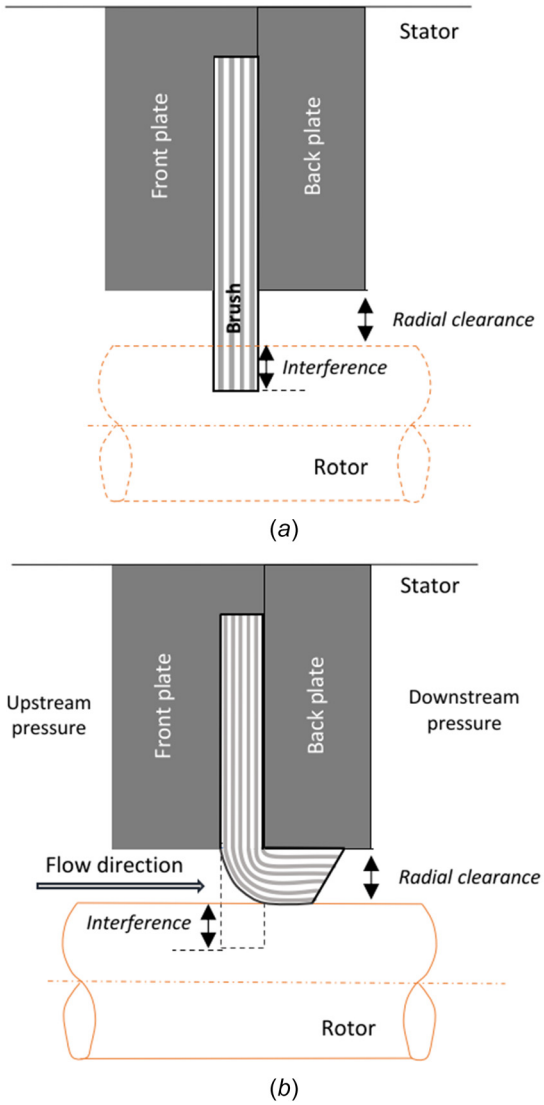

Fig. 1 Schematic representation of a carbon brush seal: (*a*) undeformed brush representation and (*b*) deformed brush representation

using the theory of flow in the porous medium created by the bristles pack [7–15]. The most advanced approaches are based on a fluid–structure interaction involving three-dimensional CFD and mechanical modeling of the brush [16].

The Kevlar brush seals design is described in Ref. [17]. They feature bristles finer than for metallic seals, of approximately 0.012 mm in diameter, providing tighter sealing and lower leakage rate. The manufacturing process ensures up to 7000 fibers per circumferential millimeter, with bristles inclined at 15 deg and maximum rotor interference of 0.2 mm [3]. These seals are limited to operating environments below 250 °C due to the thermal degradation of Kevlar bristles.

Carbon brush seals (Fig. 2) differ by their use in high-temperature applications, benefiting from the thermal and mechanical properties of carbon fibers [18]. These fibers are significantly smaller in diameter and have longer lengths than the previous two types. Carbon brush seals feature bristles with diameters as fine as 5 μm and lengths up to 2 mm. The manufacturing process involves intertwining thousands of carbon fibers into a single brush seal winding as shown in Fig. 3 [18]. This winding is then methodically coiled around a metal circular core. Once the windings are uniformly arranged around the core, positioning the fibers to naturally incline toward the center, the core is securely clamped between the front plate and the back plate.

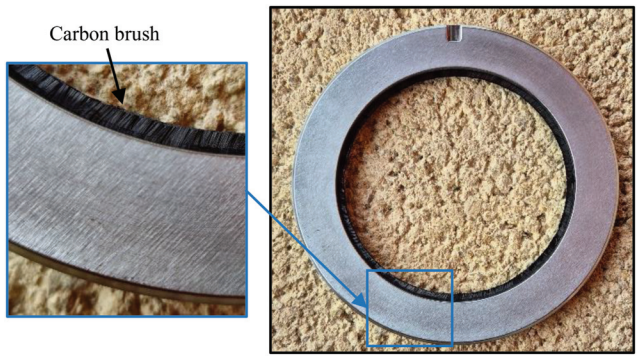

Fig. 2 Carbon brush seal sample

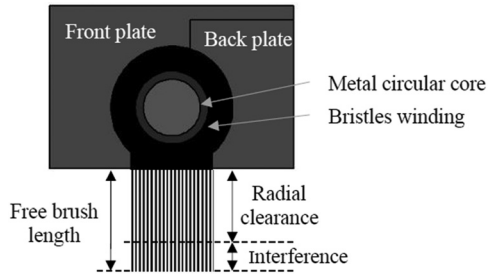

Fig. 3 Cross section of carbon brush seal

Carbon brush seals are designed to operate with an interference with the rotor up to half of the brush free length, enabling a high degree of flexibility and adaptability to surface variations and misalignments. Therefore, they allow overcoming alignment issues and radial growth transients. Capable of operating in environments with temperatures above 500 °C, carbon brush seals excel in heat dissipation due to high thermal conductivity of carbon. An additional advantage of carbon as a bristle material lies in its exceptional thermal stability, chemical inertness, and lower coefficient of friction compared to metal alloys and Kevlar. For example, Ruggiero et al. [19] tested carbon brush seals and highlighted a lower heat generation (up to 66%) than aramid brush seals.

Another significant benefit of nonmetallic brush seals is their effectiveness in minimizing mass flow leakage. The dense arrangement of small diameter, nonmetallic bristles creates a tortuous path for the fluid, significantly increasing the resistance to flow. Experimental analyses have demonstrated that nonmetallic brush seals can have leakage rate of up to an order of magnitude smaller compared to traditional labyrinth seals [20].

So far, few results are available to characterize and interpret the behavior of carbon brush seals [20,21]. The present study is an experimental and numerical analysis of their leakage characteristics. Making use of a dedicated static test rig, the relationship between rotor/brush interference and leakage flow rates is explored, alongside developing a numerical model to predict these interactions. These investigations shed light on the behavior of brush seals under four interferences between the rotor and the brush. It is found that for high interference between the bristle and the rotor, the brush does not deform that much due to the stress resulting from flow and the mass flow rate can be theoretically predicted by a porous flow model using only one parameter.

The analysis is organized as follows. In Sec. 2, the experimental setup is presented, and mass flow rates obtained for different values of the interference between the brush and the rotor are reported. A model relying on flow in porous media is employed to interpret the data. Macroscopic coefficients involved in this model are identified, and their physical implication is discussed. Section 3 is dedicated to a numerical approach based on a model structure for the brush. Results obtained with this approach are analyzed and compared to experimental data. Finally, conclusions are drawn in Sec. 4.

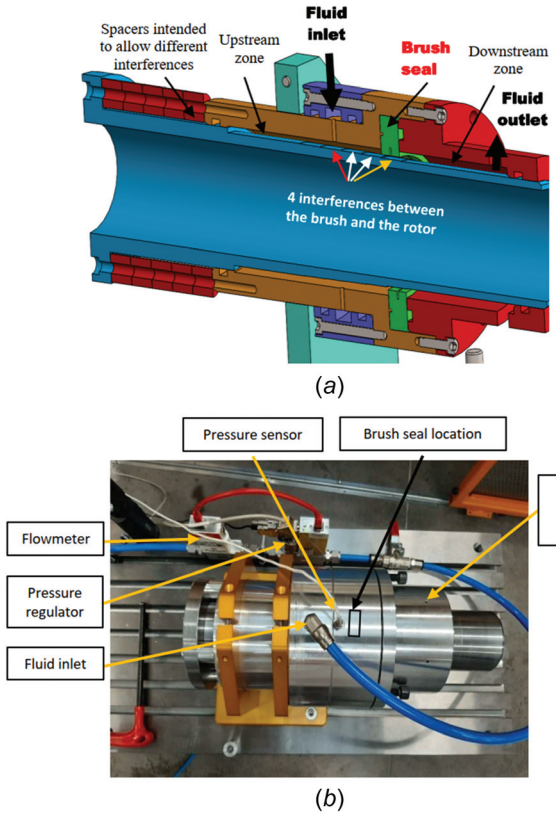

Fig. 4 Experimental test rig (*a*) and instrumentation (*b*)

2 Experimental Setup and Results

2.1 The Test Rig. A test rig developed to evaluate steady-state leakage rates for the seal without rotation is depicted in Fig. 4(*a*). The air used in the test rig was directly supplied by a pressurized vessel fed by a compressor and controlled by valve. Details of the inlet, the exit, the flowmeter, and the pressure sensor are shown on Fig. 4(*b*). Upstream pressure was controlled by a regulator mounted between the air inlet and the flowmeter. The test rig was not prone to any vibrations because measurements were carried out without rotation, in a steady-state regime. Furthermore, pressure losses related to the rig were evaluated by testing a dummy seal which replicated the geometry of the seal without its brush. The mass flow rate and the pressure measurements indicated that the fluid circulating through the experimental setup, in the absence of the brush, does not encounter significant resistance to flow. The measured mass flow rates are the result of the sealing provided by the brush without any other parasitic losses.

The rig enables testing different rotor/brush interferences with the same rotor. For this purpose, the rotor has four sections of different diameters axially offset and carefully tolerated to allow for different interferences. The brush seal is placed in a fixed position between the upstream and the downstream chambers. Modifying the axial position of the rotor makes it possible to select one of the four interferences with the brush of the same seal as shown in Fig. 4(*a*).

The length of the free undeformed brush measured radially from the front plate inner diameter to their tip is 1.95 mm. The ratios between the four interferences and the brush length were 0, 0.28, 0.34, and 0.54. They correspond to ratios between the radial clearance (measured from the front or back plate to the rotor surface) and the brush length of 1, 0.72, 0.66, and 0.46, respectively.

2.2 Measured Mass Flow Rates. Figure 5 presents experimental results of leakage tests obtained with dry air at 20 °C for a seal with a density of 24,000 bristles per millimeter of circumferential length. The seal exit was at atmospheric pressure. The

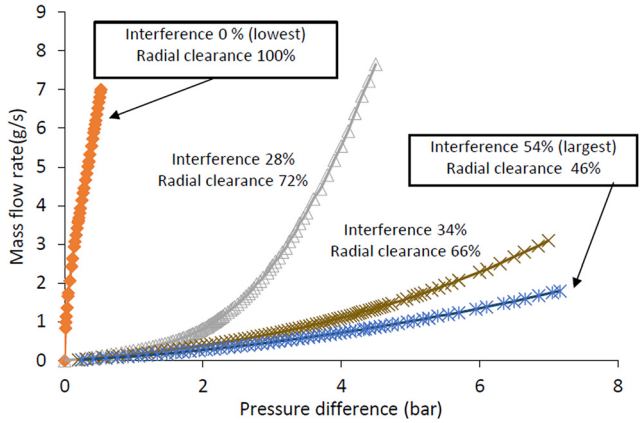

Fig. 5 Experimental mass flow rate for four interference positions

accuracy of the pressure measurements is 0.25% of full scale, i.e., 0.025 bar, and the accuracy of the measured mass flow rates is 0.1% of full scale, i.e., 0.034 g/s plus 0.5% of the reported value. Leakage flow rates vary considerably depending on the interference between the brush and the rotor. For interference 0, the radial clearance corresponds to the bristle length (the tips are barely in contact with the rotor), and the leakage flow shows a rapid increase for small variations in pressure difference. This is explained by the deformation of the brush, which does not press against the rotor and is strongly bent under the effect of the stress exerted by the fluid.

Results obtained for interference 28%, when the brush is slightly bent against the rotor, show a roughly parabolic variation with increasing pressure difference. This parabolic variation becomes less pronounced with increasing interferences. For the largest interference 54%, the variation of the leakage flow rate is almost linear. This linear variation can also be identified for interference 34% in a range of small enough pressure differences.

These results indicate that combined physical mechanisms influence the flow through the brush. With increasing interference, the radial clearance between the back plate and the rotor diminishes, and the brush is more strongly deformed between the rotor and the back plate. The deformation of the brush generates large bending displacements of the bristles that become stiffer. Stiffening due to large bending displacements is a common feature for elastic beams [22]. The brush is therefore a more rigid obstacle to flow, and it is less deformed by the fluid action resulting from the pressure difference. In addition, at sufficiently large flow rates, fluid compressibility and flow inertia effects may become significant.

2.3 Leakage Interpretation Using a Porous Medium Flow Model. The empirical Darcy–Forchheimer model for porous media flow [23] is used for interpreting the results reported in Fig. 5. This is motivated by the fact that this is the simplest and most reasonable model to represent the flow under consideration through this porous-like system. The justification of taking into account inertial effects will be provided a posteriori upon estimation of the Reynolds number values (see end of Sec. 2.4). This model extends Darcy's law, which is valid for creeping flow, and includes nonlinear inertia effects appearing with increasing flow velocities. It is given by

$$\nabla P = -\mu \boldsymbol{K}^{-1} \cdot \boldsymbol{V} - \beta \rho |\boldsymbol{V}| \boldsymbol{V} \tag{1}$$

Here, ∇P and $\boldsymbol{V}$ are, respectively, the local pressure gradient and filtration velocity within the brush considered as an equivalent homogeneous porous medium. In addition, $\boldsymbol{K}$ represents the intrinsic permeability tensor, β is the inertial resistance coefficient, whereas μ and ρ are the dynamic viscosity and density of the fluid. The Darcy–Forchheimer law represents the macroscopic form of momentum balance.

The continuity equation for a compressible fluid and the ideal gas law are

$$\nabla \cdot (\rho \boldsymbol{V}) = 0 \tag{2}$$

$$P = \rho RT/M \tag{3}$$

Here, T is the temperature, M is the molar mass, and R is the universal constant of ideal gas. By assuming a one-dimensional flow (in the axial direction), the integration of Eqs. (1) and (2) and taking Eq. (3) into account yields

$$\frac{M}{RT}\frac{P_1^2 - P_2^2}{2L} = \frac{\mu}{K}\frac{Q_m}{S} + \beta\left(\frac{Q_m}{S}\right)^2 \tag{4}$$

Here, L corresponds to the brush thickness, and S corresponds to the section area in the axial direction. Moreover, K is the diagonal component of the permeability tensor in the axial direction, Q_m is the mass flow rate, and P_1, P_2 are the upstream and downstream pressures.

The assumption of a one-dimensional flow is justified by the fact that the rotor is motionless and the bristles have no inclined (tangential) layout. Even if the local flow can be two-dimensional (axial and radial), the macroscopic radial pressure drop is zero and, therefore, the overall macroscopic flux to force description of the system reduces to an axial flow related to the axial pressure drop.

Equation (4) shows that the difference of the pressure square is a quadratic function of Q_m/S if μ/K and β are considered as constant. Figures 6 and 7 depict the experimental results represented as

$$Y = \frac{\mu}{K}X + \beta X^2 \tag{5}$$

where $Y = M/RT\left(P_1^2 - P_2^2\right)/2L$ and $X = Q_m/S$. Second order polynomial regressions were also added to the figures.

The coefficients of the linear and quadratic parts, (μ/K and β), express viscous and inertia effects in Darcy–Forchheimer's law. Any departure from a parabolic law enlightens additional effects. For example, deformation of the brush resulting from the fluid stress would affect the permeability K. Bristles deformation is expected to decrease the brush permeability, thus increasing flow resistance and pressure drop if the contact between the brush and the rotor is not lost. Nevertheless, with increasing pressure gradients, the brush may lift from the rotor, and this would create a gap between the bristle tips and the rotor. This would induce a much larger leakage path with a far smaller resistance to flow than that through the brush itself. This combined leakage paths must be considered when analyzing the flow characteristics and associated pressure losses.

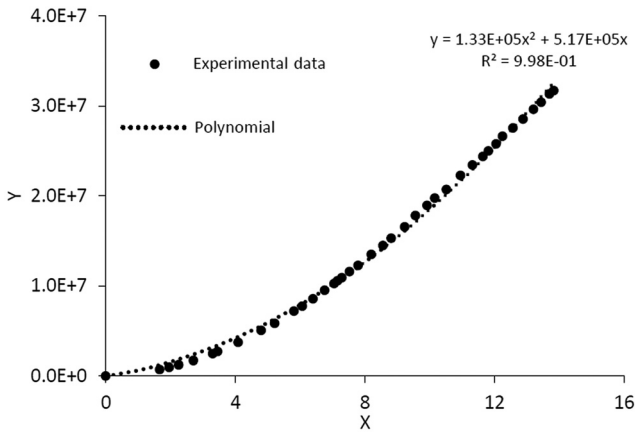

Fig. 6 Parameters of the Darcy–Forchheimer model for interference 0% (lowest)

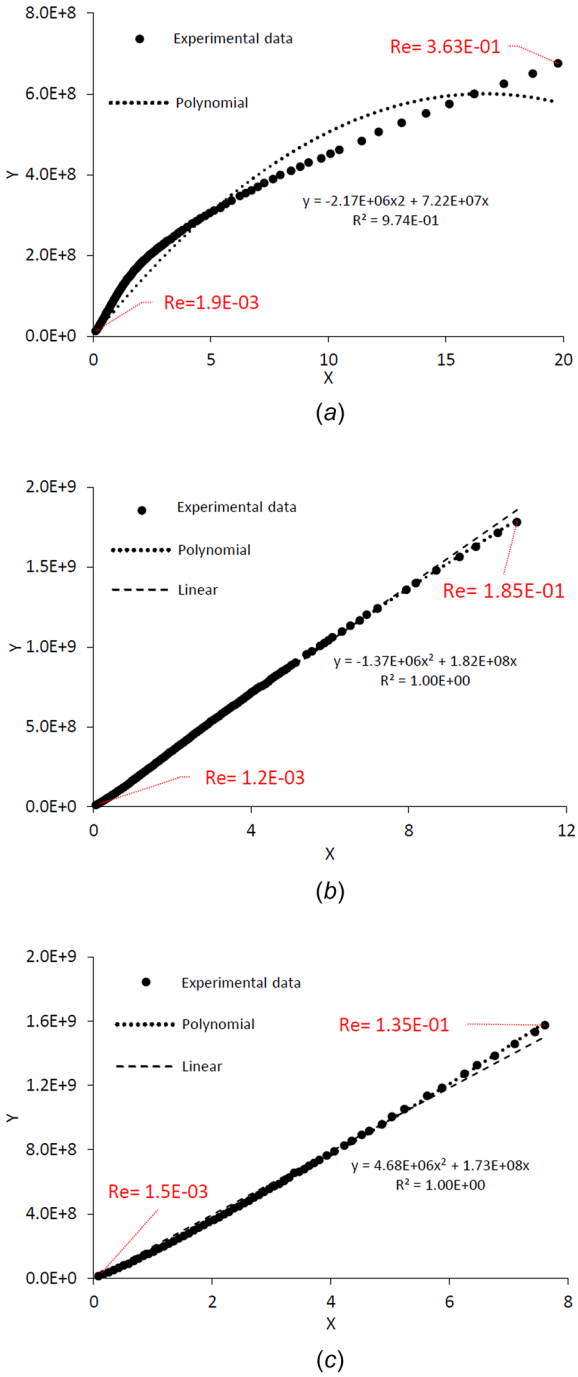

Fig. 7 Parameters of the Darcy–Forchheimer model: (*a*) interference 28%, (*b*) interference 34%, and (*c*) interference 54%

Results reported in Fig. 6 correspond to a situation where the brush fills in the radial clearance without interference between the bristles and the rotor. A progressive deviation from a linear variation $Y = \mu/K \cdot X$ appears with increasing values of Y (related to the pressure drop) and X (related to the flow rate). This can be interpreted as dominant inertia effects, possibly combined with the brush deformation and flow through an open clearance.

Results represented in Fig. 7(*a*) are obtained for 28% of the brush length interference with the rotor. A linear variation of Y (the squared pressure difference) with X (the mass flow rate) is visible up to a low-pressure difference of 0.5 bar. Beyond this value, the results show a strongly, nonlinear variation that can be attributed to the loss of interference between the brush and the rotor.

Figure 7(*b*) depicts the results for 34% interference of the brush length with the rotor. They show a linear variation of Y up to values corresponding to a pressure difference of 6 bar. After this limit, the results show a parabolic variation with a negative inertial resistance coefficient, which is not physically meaningful. It may be argued that, as for Fig. 7(*a*), the negative value of this coefficient results from a complex interplay between the brush deformation and a small loss of the interference effects.

Figure 7(*c*) depicts the results obtained for 54% interference of the brush length with the rotor. For this significant interference, $Y(X)$ follows accurately the variation predicted by Eq. (5) over the entire range of pressure drop values. The brush deformation induced by the fluid flow is strongly reduced due to the stiffness increase of the brush compacted between the rotor and the back plate. The positive quadratic coefficient indicates that compressible flow with inertia effects is reasonably well represented by Eq. (5). Inertial flow effects thus dominate over brush deformations induced by the fluid stress applying onto the bristles.

In summary, these observations highlight the distinctions and complex interplay between the effects of brush deformation and porous medium flow.

From the above results, the Reynolds number, defined as $\mathrm{Re} = (\rho|V|\sqrt{K})/\mu = (Q_m\sqrt{K})/\mu S$, can be evaluated. The maximum values of this number for interferences 28%, 34%, and 54% are 3.63×10^{-1}, 1.85×10^{-1}, and 1.35×10^{-1}, respectively. This indicates that inertial effects are indeed expected (see, for instance, Ref. [24]) justifying the consideration of the Darcy–Forchheimer model of Eq. (4).

2.4 Evaluation of the Permeability and Inertial Resistance Coefficient. The permeability, K, and inertial resistance coefficient, β, used in Eq. (5) can be evaluated by fitting a polynomial least square regression to experimental data. Regressions can be made by using all experimental data as in Figs. 6 and 7 or by progressively expanding the dataset to include all points, from small to large feeding pressures. The latter approach makes it possible to highlight the phenomena that gradually come into play.

Figure 8 depicts the identified permeability values versus pressure difference. Measurements performed without interference were not considered in this analysis since, in that case, it was considered that the brush was not in contact with the rotor.

Results obtained for the lowest interference (28%) show a rapid increase in permeability for a pressure difference larger than 2 bar. This result can be considered to be due to a significant loss of contact between the brush and the rotor. Values of the permeability for pressure differences lower than 2 bar show a rapid decrease that indicates a strong modification of the brush shape before liftoff.

A consistent trend is observed for larger interferences (34% and 54%): the permeability decreases with increasing pressure in agreement with an increasing resistance to fluid flow. Also, higher

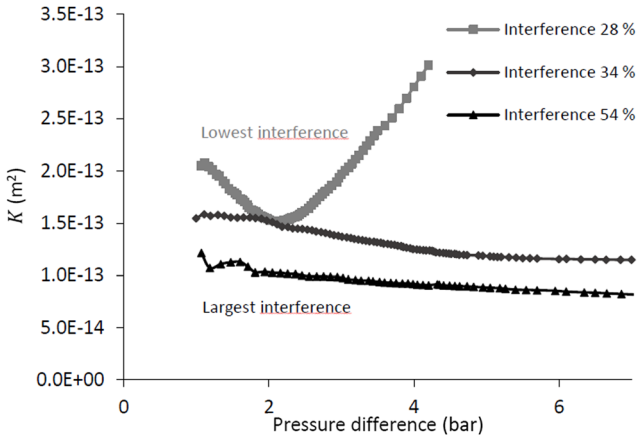

Fig. 8 Variation of the experimentally identified permeability

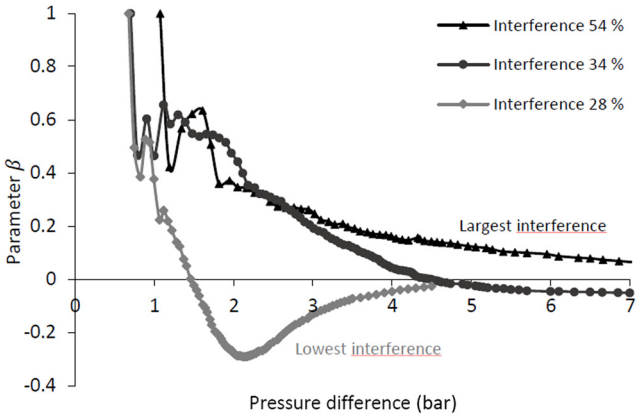

Fig. 9 Variation of the experimentally identified inertial resistance coefficient

interferences between the brush and the rotor result in lower permeability values at a given pressure difference. This can be explained by a compaction effect of the bristles of the brush in the radial clearance between the back plate and the rotor that increases with the interference.

In Fig. 9, the variation of the inertial resistance coefficient β is reported versus the pressure difference. As stated above, measurements performed without interference were not considered in this analysis.

The inertial resistance coefficient β obtained for the lowest interference (28%) shows a rapid decrease and becomes negative beyond a pressure difference of 1.5 bar. A negative value for β indicates that the model given by Eq. (1) or (4) is no longer valid. As previously mentioned, this can be attributed to a significant loss of contact between the brush and the rotor. A similar behavior is obtained for the 34% interference as the inertial resistance coefficient becomes slightly negative for pressure differences larger than 4.5 bar. However, the variations are much smaller and indicate a small progressive loss of contact between the brush and the rotor. Values at which the liftoff occurs are significantly larger than for the 28% interference, which is consistent with the stiffness increase of the brush.

For 54% interference, the inertial resistance coefficient remains positive over the whole range of pressure differences explored in the experiments and decreases with increasing feeding pressure. For this interference, it is understood that the contact between the brush and the rotor is preserved for all pressure differences, and the model described by Eq. (1) or (4) is fully valid. Moreover, the inertial resistance coefficients tend to a constant value which is in accordance with the fact that the shape of the brush no longer changes.

3 The Numerical Model

The domain and boundary conditions for the numerical flow analysis through the brush are depicted in Fig. 10. A nonporous fluid domain is added upstream and downstream of the brush to allow realistic boundary conditions to be imposed.

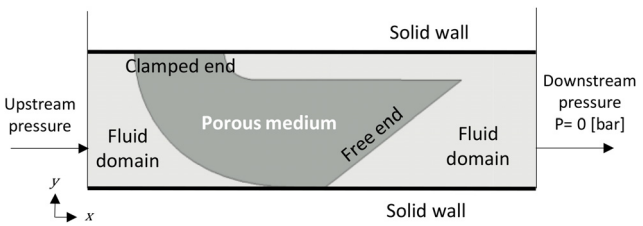

Fig. 10 The macroscopic boundary conditions

Compressible, isothermal, steady flow is assumed. The gas obeys ideal gas law so that the mass conservation equation and state law of the ideal gas are those given in Eqs. (2) and (3). For momentum conservation, the Darcy–Forchheimer Eq. (1) is extended by incorporating viscous diffusion yielding a Darcy–Brinkman–Forchheimer model that writes

$$-\nabla\cdot\left(\frac{\mu}{\phi}(\nabla\mathbf{V}+\nabla\mathbf{V}^{T})-p\mathbf{I}\right)+\mu\boldsymbol{K}^{-1}\cdot\boldsymbol{V}+\rho\beta|\boldsymbol{V}|\boldsymbol{V}=0 \quad (6)$$

Here, ϕ is the porosity of the porous medium. The advantage of this approach is that the flow description can be made with a single model using a so-called penalization method [25,26]. Indeed, in the pure fluid regions, $\boldsymbol{K}$ can be set to an extremely large value, ϕ to 1 and β to zero to recover the Stokes model. The boundary conditions are such that high and low pressures are imposed at the upstream and downstream boundaries, whereas a zero velocity is imposed at the upper and lower boundaries (Fig. 10). Moreover, the flow is assumed to be axisymmetric.

As shown in Fig. 10, the brush deforms following its placement in the radial clearance between the rotor and the back plate of the seal. At one end, the bristles are clamped between the front and back plates and form a compact network. Bristles gradually separate toward the free end. To carry out the simulation, the distance between the bristles at the free end is assumed to be constant. Moreover, it is also assumed that the distance between the bristles varies linearly from zero at the clamped end to a value D_p at the free end. Deformation of the bristles is not supposed to be impacted by the leakage flow. Furthermore, the contacts between the bristles are ignored.

Boundaries delimiting the porous domain that constitutes the brush are obtained by assuming that the bristles deform as beams. The ratio between their length and diameter is 400. Bristles deformed as beams are computed by a finite element model inspired from Kirchhoff's theory which employs third order Hermitian shape functions in order to account for large deformations [27]. It is assumed that bristles deformation is due to their interference with the rotor, and this contact problem was solved using the penalty method.

In Fig. 11, the deformation of a bristle with one clamped end and different interferences with the rotor is represented versus the distance along the rotor axis. Two types of contacts are obtained. For interferences not exceeding approximately half the bristle length, point contacts occur between the free end and the rotor surface. With increasing values of the interference, part of the bristle near its tip lays against the rotor resulting in a line-to-line contact.

Deformation of the first, upstream bristle is governed only by its interference with the rotor, whereas, for the last downstream bristle, the spacing between the bristles in the pack must also be considered.

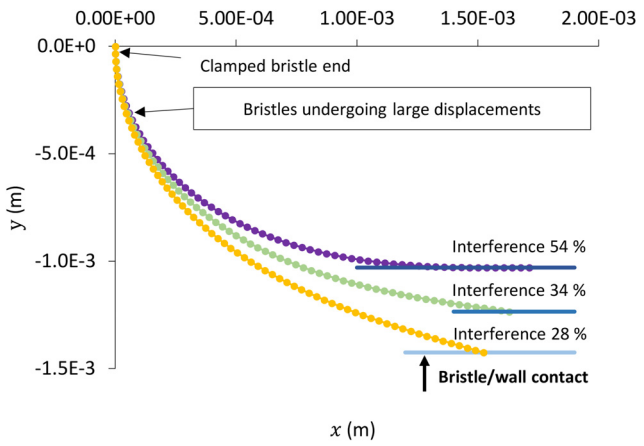

Fig. 11 Bristle undergoing large displacements engaging a contact with a wall

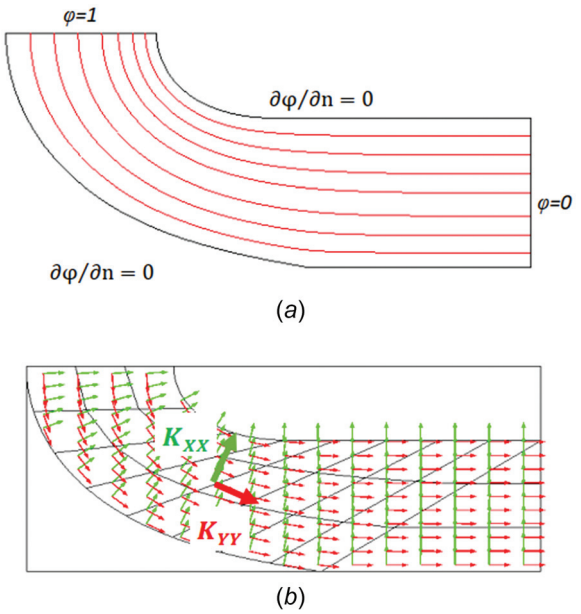

Fig. 12 Boundary conditions for the solution on φ of the Laplace problem (*a*) and the resulting local curvilinear coordinate system (*b*)

The deformation of the brush leads to a strongly heterogeneous porosity field, ϕ, that can be estimated in a local coordinate system that approximately follows the direction of the bristles, as shown in Fig. 12.

This local coordinate system is defined from the solution of a diffusion boundary value problem on a potential variable, φ, i.e., by solving Laplace equation, $\Delta\varphi=0$, in the domain depicted in Fig. 12(*a*) with zero wall flux boundary conditions, $\partial\varphi/\partial n=0$.

The solution to this problem yields the potential φ, whose derivatives, $\partial\varphi/\partial y$ and $-\partial\varphi/\partial x$ in the global Cartesian system of coordinates (x,y), are the components of a conservative velocity vector. The corresponding vector field is represented as red arrows in Fig. 12(*b*) and approximately describes the direction of the bristles. A simple rotation gives the corresponding orthogonal vector field, depicted as arrows in Fig. 12(*b*).

These vector fields define a local system of coordinates, *XYZ*, aligned with the deformed bristles at each point within the brush. The *X*, *Y*, and *Z* directions can therefore be reasonably considered as the principal directions of the local permeability tensor. The principal values of the permeability tensor, K_{XX}, K_{YY}, and K_{ZZ} can then be computed in the local longitudinal (*Y*) and transverse (*X* and *Z*) directions. These components are determined in a representative cell extracted from bristles arranged in a square centered structure as shown in Fig. 13. The choice of such an arrangement is justified by the fact that, at the clamped edge, bristles are organized in a very compact pattern, close to this structure.

The side lengths of the representative cell at the clamped edge are

$$l_{X0}=l_{Z0}=d\sqrt{2} \quad (7)$$

while at the free end these values are

$$l_{X1}=l_{Z1}=(d+D_p)\sqrt{2} \quad (8)$$

as depicted in Fig. 14(*a*).

The porosity is

$$\phi=1-\frac{\pi}{4}\left(\frac{d}{d+D_p}\right)^2 \quad (9)$$

varying from $\phi_{\min}=0.215$ at the clamped end to its maximum value at the free end. This corresponds to a linear variation of D_p from zero

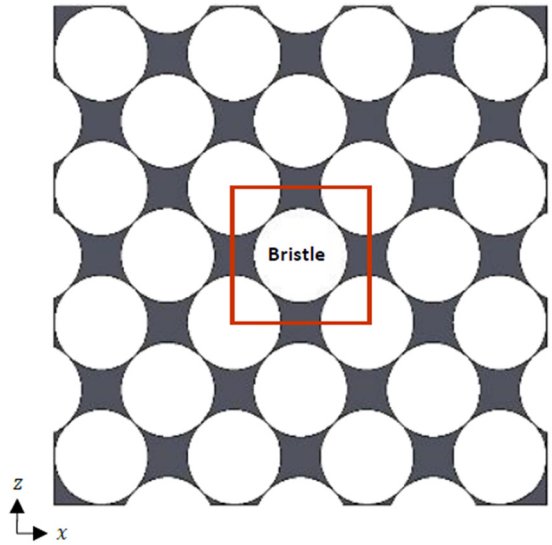

Fig. 13 Square centered bristle arrangement at the brush clamped end

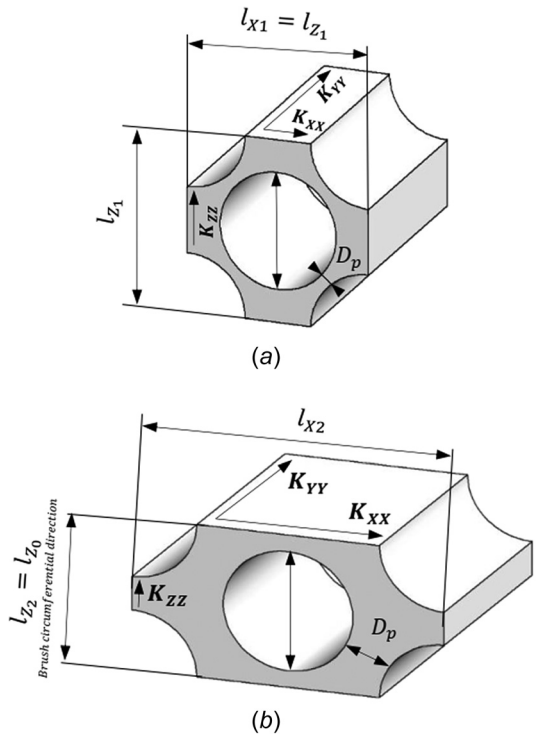

Fig. 14 Square centered (top) (*a*) and rectangular centered (bottom) (*b*) bristle periodic cells along the brush

to an imposed value. The representative unit cell depicted in Fig. 14(*a*) enables the computation of the three components, K_{XX}, K_{YY}, and K_{ZZ}, K_{XX} and K_{ZZ} being equal for symmetry reasons.

The permeability tensor in the local coordinate system XYZ varies along the bristles length. A rotation $\boldsymbol{R}$ of this tensor provides the permeability tensor in the global Cartesian system of coordinates xyz according to the following relationship:

$$\begin{bmatrix} K_{xx} & K_{xy} & K_{xz} \\ K_{yx} & K_{yy} & K_{yz} \\ K_{xz} & K_{yz} & K_{zz} \end{bmatrix} = \boldsymbol{R}^T \begin{bmatrix} K_{XX} & 0 & 0 \\ 0 & K_{YY} & 0 \\ 0 & 0 & K_{ZZ} \end{bmatrix} \boldsymbol{R} \tag{10}$$

Here, $\boldsymbol{R}$ is the rotation matrix given by

$$R = \begin{bmatrix} \cos\alpha & \sin\alpha & 0 \\ -\sin\alpha & \cos\alpha & 0 \\ 0 & 0 & 1 \end{bmatrix} \tag{11}$$

where α is the local rotation angle.

When transposing the representative cell to the brush seal, l_X and l_Z correspond to unit cell sizes in the radial and circumferential directions, respectively. Since bristles spacing is constrained in the circumferential direction at a given distance from the contact with the rotor, it is more realistic to consider l_Z constant and equal to its value at the clamped end (i.e., $l_{Z2} = l_{Z0}$) and only allow l_X to vary. This leads to the second model of representative unit cell depicted in Fig. 14(*b*) with

$$\begin{aligned} l_{X2} &= \sqrt{4(d + D_p)^2 - 2d^2} \\ \phi &= 1 - \frac{\pi}{4} \frac{d}{\sqrt{2(d + D_p)^2 - d^2}} \end{aligned} \tag{12}$$

The stretching in the X-direction is expected to significantly increase K_{XX} (and K_{YY}) which are the only two principal values computed on the unit cell that contribute to K_{xx} and K_{yy} after application of the rotation operator given in Eq. (10). In other words, K_{ZZ} plays no role in the overall leak-rate process, as expected, preserving the axisymmetric character of the flow.

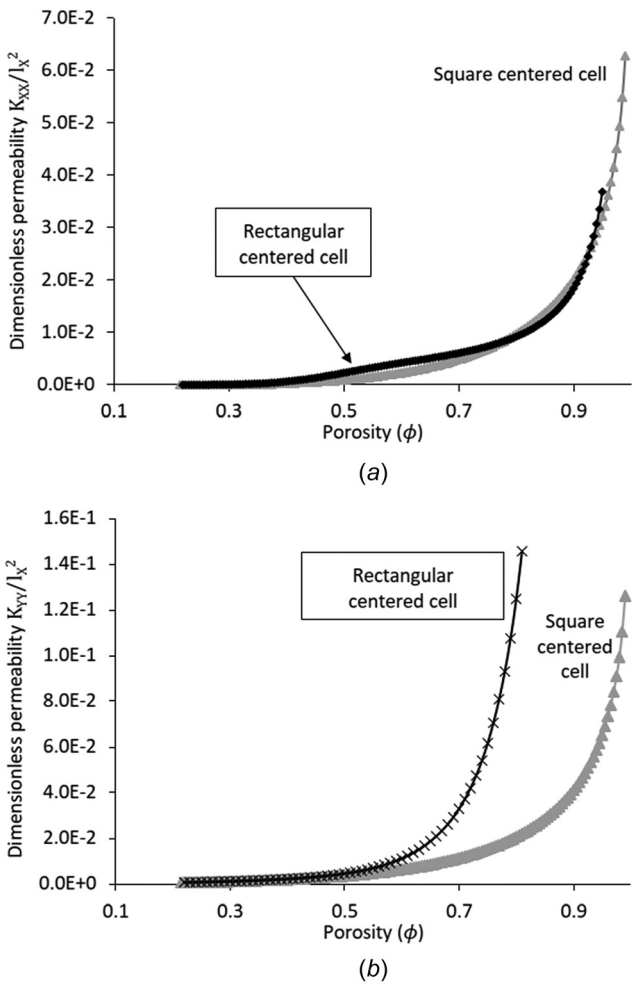

Fig. 15 Permeability coefficients K_{XX} (*a*) and K_{YY} (*b*) in the local system of coordinates made dimensionless by l_x^2 versus porosity

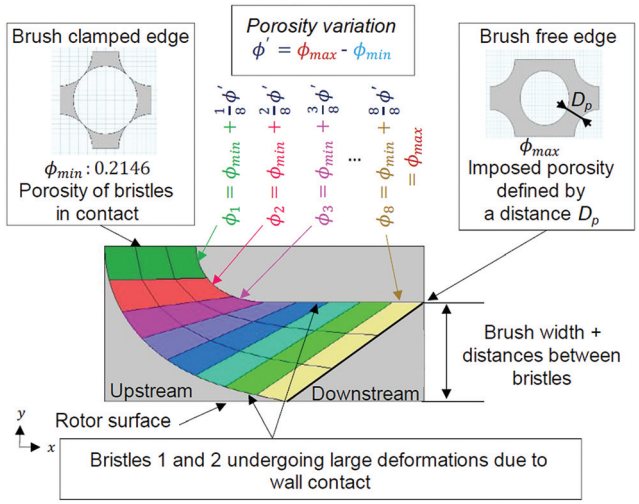

Fig. 16 Macroscopic model domain definition

Both representative cells depicted in Fig. 14 can be used for calculating the permeability.

The permeability coefficients are determined from the solution of the closure problem that results from upscaling the creeping incompressible flow problem in a rigid periodic structure. This can be obtained from double-scale periodic homogenization [28], volume averaging [29], or the adjoin and Green's formulation [30–32]. The closure problem, in which the closure variables $\mathbf{d}$ (m) and $\boldsymbol{D}$ (m^2) are, respectively, a vector and a second order tensor, is given by

$$\begin{aligned} \nabla \cdot \boldsymbol{D} &= 0 \\ -\nabla \mathbf{d} + \nabla^2 \boldsymbol{D} + \boldsymbol{I} &= 0 \end{aligned} \tag{13}$$

with $\boldsymbol{D} = 0$ at the solid–fluid boundary, whereas $\mathbf{d}$ and $\boldsymbol{D}$ are X and Z-periodic and $\mathbf{d} = 0$. Here, $\langle\rangle$ stands for the average over the representative cell. After numerically solving Eq. (13), the permeability tensor is obtained as

$$K = \langle \boldsymbol{D} \rangle \tag{14}$$

An example of the permeability coefficients K_{XX} and K_{YY}, scaled by l_X^2, is reported in Figs. 15(*a*) and 15(*b*) for square centered and rectangular centered unit cells. As expected, K_{XX}/l_x^2 is not significantly modified, whereas K_{YY}/l_x^2 strongly increases when the unit cell is stretched in the X direction. With this representation of the local bristles structure at hand, the permeability of the brush, considered as an heterogeneous material, is explored in Sec. 4.

4 Results

The porous region representing the brush in the computational domain is divided into equally spaced discretization elements along and across the deformed brush as shown in Fig. 16. Each element has a different porosity set by a linear variation of D_p. The values of the permeability coefficients, K_{XX} and K_{YY}, of each element are first computed in the local system of coordinates and are expressed in the global system of coordinates after application of the rotation expressed in Eq. (10). Continuity of the pressure and flux is applied between each element. The leakage flow rate is finally computed by integrating the mass flux at the upstream (or downstream) boundary of the computational domain. For the sake of simplicity, the inertial resistance coefficient β is set from the experimental data shown in Fig. 9 by averaging the positive values on the simulated pressure range.

A verification was carried out by doubling the number of equally spaced discretization elements in both directions. This showed no significant impact of the grid refinement on the mass flow rate, indicating that the chosen discretization is adequate.

An example of the pressure field obtained from the flow solution (Eqs. (2), (3), and (6) and associated boundary conditions) is represented in Fig. 17. The converging shape resulting from the contact between the brush and the rotor surface causes a narrowing of the flow at this specific location. This narrowing has the effect of locally increasing the fluid velocity as well as the pressure within the seal. This increase in pressure can lead to the lifting of the brush when the pressure reaches a threshold.

This lifting of the brush impairs the performance of the seal as a result of the leak-rate increase as inferred from the experimental results reported in Secs. 2.3 and 2.4.

The analysis of the pressure isolines reveals a progressive drop in pressure in the upward direction normal to the bristles of the brush. This pressure drop results in an acceleration of the fluid flow through the brush, thereby leading to an increase in the leak-rate. The pressure distribution observed in the model confirms the suitability of the adopted local coordinate system.

The mass flow rates versus the inlet–outlet pressure differences are depicted in Figs. 18(*a*)–18(*c*) corresponding to interferences of 28%, 34%, and 54%, respectively. The dimensionless distance between bristles at the free end is $\bar{D}_p = D_p/d$.

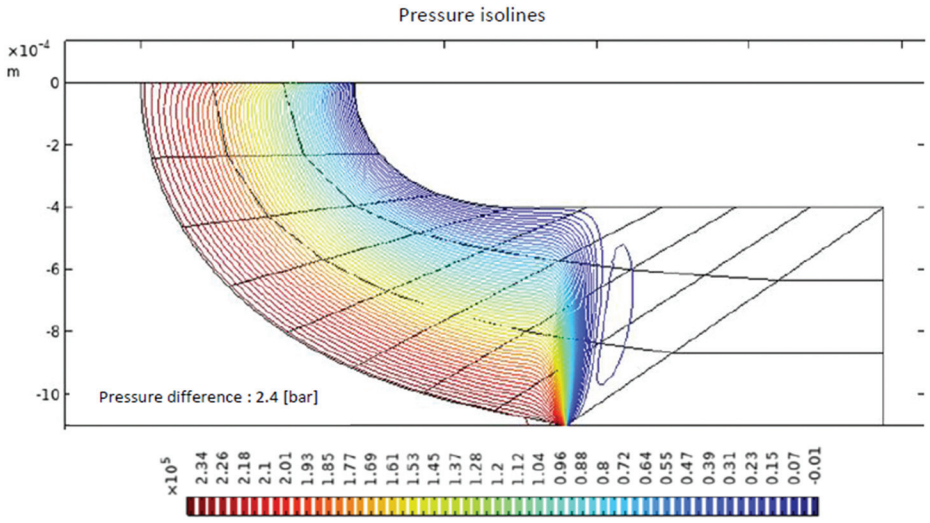

Fig. 17 Pressure isolines

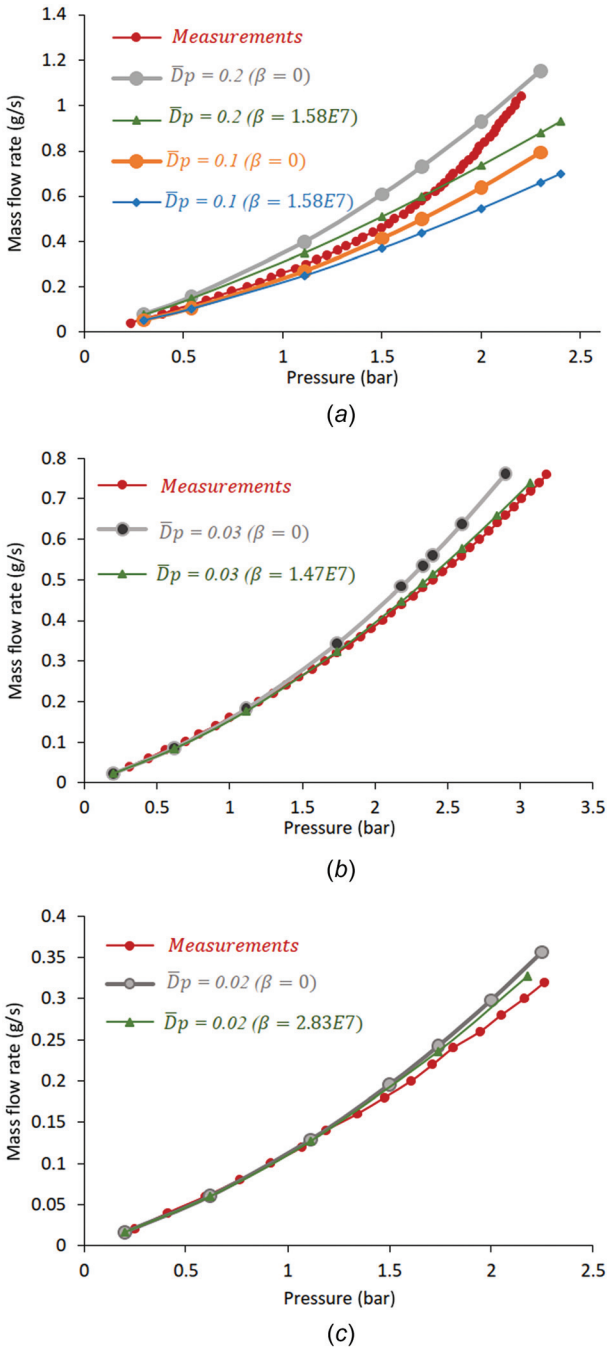

Fig. 18 Comparison between experimental and numerical mass flow rates as functions of the pressure difference: (*a*) interference 28%, (*b*) interference 34%, and (*c*) interference 54%

For an interference of 28%, the values of the dimensionless distance between bristles, $\bar{D}_p$, were varied in a range between 0.1 and 0.2. The largest differences between the predictions and the experimental results are observed for this interference. These differences can be attributed to significant deformations of the brush under the influence of flow forces, a mechanism that is not taken into account in the present model. Moreover, the possibility of bristles lifting at high pressure values could result in an additional flow path between the brush and the rotor, further complicating the flow analysis. As was already mentioned before, the fluid–structure interaction is an important aspect that seems to be dominant for this interference. Indeed, as can be observed from Fig. 18(*a*), the agreement with experimental data is better while taking $\bar{D}_p = 0.1$ in the lower range of pressure drop (up to 1.5 bar), whereas the introduction of the inertial effects does not improve the prediction from the model. For larger pressure drops, predictions with $\bar{D}_p = 0.2$ are slightly closer to experimental observations. This is a strong indication that deformation of the brush under the action of the stress exerted by the fluid is prominent for this interference.

Conversely, numerical results show excellent agreement with the experimental data for the 34% interference, and $\bar{D}_p = 0.03$, as shown in Fig. 18(*b*). Indeed, computed flow rates closely overlap with those obtained experimentally on the whole range of investigated pressure difference, highlighting the relevance of the model in this configuration. This agreement emphasizes that the discrepancy observed in the previous part of the model was likely due to additional inertia effects, possibly combined with brush deformation induced by the flow that were not taken into account. The integration of the former into the current model has improved the correspondence between numerical predictions and experimental data. This improvement in flow prediction for the 34% interference suggests that inertia is likely to play a significant role in an accurate description of the leak through the brush seal, in particular in the upper range of the pressure difference.

The results obtained for 54% interference are depicted in Fig. 18(*c*) and confirm that the integration of inertia effects slightly improves the predictions compared to experimental data, more specifically in the upper range of the pressure difference. The maximum error between numerical results and experimental measurements obtained when $\bar{D}_p = 0.02$ is reduced to 6.5%, compared to 7% observed when inertia effects were not considered. Although this improvement is minor, it indicates a better fit of the model to experimental reality. However, it is important to note that, even with this improvement, the numerical leak flow rate results for this position still tend to slightly overpredict the experimental data. This suggests that brush deformation may still not be appropriately captured and the structure may also be oversimplified, in addition to the possible effects of brush deformation due to fluid stress resulting from flow. All these effects may be accounted for by a more thorough analysis of the fluid–bristles interaction, that is however beyond the present work dedicated to a phenomenological study of the macroscopic brush seal behavior.

5 Conclusion

The present study proposes a close look at how brush seals with long carbon fibers behave, both by observing actual seals in leakage experiments and by using theoretical models to predict their leakage flow rate. It is found that, when the seal and the rotor fit more tightly together, i.e., for high interference between the bristle and the rotor, the brush does not deform that much due to the stress resulting from flow. Large bending of the brush in the space between the back plate and the rotor plays an important role in leakage flow rate of the seal. Indeed, this contributes to increase the brush stiffness, that is therefore less prone to deform under the action of the stress exerted by the fluid. This is confirmed by the set of experiments reported in this work that show how the leak-rate changes with different levels of interference, and how the deformation does not play a significant role in the interpretation of the leak-rate results using a Darcy–Forchheimer model. The developed theoretical model better predicts the observed leakage flow rates for the largest interferences considered here. In view of the above conclusions, it clearly appears that a more accurate prediction a flow rate through the brush seal would require incorporating the fluid structure interaction, at least when the interference is not large enough for the brush stiffness to be larger than the typical fluid stress. This is undoubtedly a difficult task that was out of the scope of the present work dedicated to a phenomenological characterization of a brush seal behavior. Nevertheless, a practical recommendation for an efficient use of a brush seal is to mount it with enough interference (compatible with other constraints in terms of wear and resistance due to the brush/rotor friction) to avoid this effect that is detrimental to the seal efficiency. While this work gives valuable insights into designing

more efficient carbon brush seals, the next step will be the investigation of the leak-rate with rotor speed and vibrations.

Acknowledgment

The authors would like to acknowledge the support of CETIM and Technetics Group France SAS for this work.

Funding Data

- CETIM and Technetics Group France SAS.

Data Availability Statement

The datasets generated and supporting the findings of this article are obtainable from the corresponding author upon reasonable request.

Nomenclature

D_p = distance between bristles, m
$\boldsymbol{K}$ = intrinsic permeability of the medium, m^2
l = length of the representative cell
L = characteristic length, m
M = molar mass, kg/mol
P = pressure, Pa
Q_m = mass flow rate, kg/s
R = ideal gas constant, 8.314 J/mol/K
$\boldsymbol{R}$ = rotation matrix
S = flow section, m^2
T = temperature, K
V = Darcy's filtration velocity, m/s
xyz = global coordinate system
XYZ = local coordinate system

Greek Symbols

α = rotation angle
β = inertial resistance coefficient (Forchheimer term)
μ = dynamic viscosity, Pa·s
ρ = density, kg/m^3
ϕ = porosity

References

[1] Ferguson, J., 1988, "Brushes as High Performance Gas Turbine Seals," ASME Paper No. 88-GT-182.
[2] Bowen, J. P., Bird, J. J., Cross, H., Jenkins, M. R., Bowsher, A. A., Crudgington, P. F., Sangan, C. M., and Scobie, J. A., 2024, "Fluid Dynamic Behaviour of Conventional and Pressure Relieving Brush Seals," ASME J. Eng. Gas Turbines Power, **146**(6), p. 061001.
[3] Flouros, M., Stadlbauer, M., Cottier, F., Proestler, S., and Beichl, S., 2013, "Transient Temperature Measurements in the Contact Zone Between Brush Seals of Kevlar and Metallic Type for Bearing Chamber Sealing Using a Pyrometric Technique," ASME J. Eng. Gas Turbines Power, **135**(8), p. 081603.
[4] Hendricks, R., Schlumberger, S., Braun, M., Choy, F., and Mullen, R., 1991, "A Bulk Flow Model of a Brush Seal System," ASME Paper No. 91-GT-325.
[5] Hendricks, R., Braun, M., Canacci, V., and Mullen, R., 1991, "Paper IX (i) Brush Seals in Vehicle Tribology," Tribol. Ser., **18**, pp. 231–242.
[6] Chupp, R., and Dowler, C., 1991, "Simple Leakage Flow Model for Brush Seals," AIAA Paper No. 91-1913.
[7] Chupp, R. E., and Holle, G., 1996, "Generalizing Circular Brush Seal Leakage Through a Randomly Distributed Bristle Bed," ASME J. Turbomach., **118**(1), pp. 153–161.
[8] Chew, J., and Hogg, S., 1997, "Porosity Modeling of Brush Seals," ASME J. Tribol., **119**(4), pp. 769–775.
[9] Turner, M. T., Chew, J. W., and Long, C. A., 1998, "Experimental Investigation and Mathematical Modeling of Clearance Brush Seals," ASME J. Eng. Gas Turbines Power, **120**(3), pp. 573–579.
[10] Dogu, Y., 2005, "Investigation of Brush Seal Flow Characteristics Using Bulk Porous Medium Approach," ASME J. Eng. Gas Turbines Power, **127**(1), pp. 136–144.
[11] Pröstler, S., 2005, *Modellierung Und Numerische Berechnungen von Wellenabdichtungen in Bürstenbauart*, University of Bochum, Verlag Dr. Hut, Bochum, Germany.
[12] Guardino, C., and Chew, J. W., 2005, "Numerical Simulation of Three-Dimensional Bristle Bending in Brush Seals," ASME J. Eng. Gas Turbines Power, **127**(3), pp. 583–591.
[13] Pugachev, A. O., and Helm, P., 2009, "Calibration of Porous Medium Models for Brush Seals," Proc. Inst. Mech. Eng. Part J. Power Energy, **223**(1), pp. 83–91.
[14] Neef, M., Hepermann, F., Sürken, N., and Schettel, J., 2007, "Brush Seal Porosity Modeling: Applicability and Limitations," Seventh European Conference on Turbomachinery, Athens, Greece, Mar. 5–9, Paper No. 110.
[15] Deville, L., and Arghir, M., 2018, "Theoretical Analysis of Brush Seals Leakage Using Local Computational Fluid Dynamics Estimated Permeability Laws," ASME J. Eng. Gas Turbines Power, **140**(6), p. 062803.
[16] Lelli, D., Chew, J. W., and Cooper, P., 2006, "Combined Three-Dimensional Fluid Dynamics and Mechanical Modeling of Brush Seals," ASME J. Turbomach., **128**(1), pp. 188–195.
[17] Gail, A., and Beichl, S., 2003, "The MTU Brush Seal Design," MTU Aero Engines, Munich, Germany, accessed July 1, 2024, http://wwwmtude/en/technologies/engineering_news/production/Gail_MTU_brush_seal_designpdf
[18] Guimet, L., Sauvinet, F., Constant, O., Reynaud, P., Mengelle, C., and Lefrancois, M., 2013, "Brush-Type Circular Seal," Patent No. 9,157,531, Commissariat à l'énergie atomique et aux énergies alternatives (Paris), Technetics Group France SAS (Saint Etienne).
[19] Ruggiero, E., Allen, J., and Lusted, R., 2008, "Heat Generation Characteristics of a Carbon Fiber Brush Seal," AIAA Paper No. 2008-4508.
[20] Outirba, B., and Hendrick, P., 2014, "Experimental Testing of Carbon Brush Seals for Aero Engines Bearing Chambers," ASME Paper No. GT2014-25684.
[21] Changizi, A., Stiharu, I., Outirba, B., and Hendrick, P., 2021, "Mathematical Model of Brush Seals for Gas Turbine Engines: A Nonlinear Analytical Solution," Adv. Mech. Eng., **13**(9), pp. 1–12.
[22] Reddy, J. N., 2015, *An Introduction to Nonlinear Finite Element Analysis*, Oxford University Press, Oxford, UK.
[23] Forchheimer, P., 1901, "Wasserbewegung Durch Boden," Z. Ver. Dtsch. Ing., **45**(50), pp. 1781–1788.
[24] Elmkies, P., Lasseux, D., Bertin, H., Pichery, T., and Zaitoun, A., 2002, "Polymer Effect on Gas/Water Flow in Porous Media," SPE/DOE 13th Symposium on Improved Oil Recovery, Tulsa, OK, Apr. 13–17, Paper No. SPE 75160.
[25] Neale, G., and Nader, W., 1974, "Practical Significance of Brinkman's Extension of Darcy's Law: Coupled Parallel Flows Within a Channel and a Bounding Porous Medium," Can. J. Chem. Eng., **52**(4), pp. 475–478.
[26] Bruneau, C.-H., Lasseux, D., and Valdés-Parada, F. J., 2020, "Comparison Between Direct Numerical Simulations and Effective Models for Fluid-Porous Flows Using Penalization," Meccanica, **55**(5), pp. 1061–1077.
[27] Meier, C., Popp, A., and Wall, W. A., 2015, "A Locking-Free Finite Element Formulation and Reduced Models for Geometrically Exact Kirchhoff Rods," Comput. Methods Appl. Mech. Eng., **290**, pp. 314–341.
[28] Auriault, J.-L., Boutin, C., and Geindreau, C., 2010, *Homogenization of Coupled Phenomena in Heterogenous Media*, Vol. 149, Wiley, Hoboken, NJ.
[29] Whitaker, S., 2013, *The Method of Volume Averaging*, Vol. 13, Springer Science & Business Media, Berlin, Germany.
[30] Bottaro, A., 2019, "Flow Over Natural or Engineered Surfaces: An Adjoint Homogenization Perspective," J. Fluid Mech., **877**, p. P1.
[31] Lasseux, D., Valdés-Parada, F. J., and Bottaro, A., 2021, "Upscaled Model for Unsteady Slip Flow in Porous Media," J. Fluid Mech., **923**, p. A37.
[32] Lasseux, D., and Valdés-Parada, F. J., 2022, "A Macroscopic Model for Immiscible Two-Phase Flow in Porous Media," J. Fluid Mech., **944**, p. A43.